AIAA JOURNAL
Vol. 45, No. 1, January 2007

Development of Hybrid Simulation for Supersonic Chemical Oxygen–Iodine Laser

Masamori Endo*
Tokai University, Hiratsuka 259-1292, Japan
and
Taizo Masuda† and Taro Uchiyama‡
Keio University, Yokohama 223-8522, Japan

DOI: 10.2514/1.20339

A numerical simulation method for a supersonic chemical oxygen–iodine laser is developed. The model is a combination of a three-dimensional computational fluid dynamics code without kinetics and a detailed one-dimensional, multiple-leaky-stream-tubes kinetics code. In the proposed method, the detailed flowfield characteristic is calculated by solving a full Navier–Stokes equation that does not involve chemical reactions, and the resultant temperature, velocity, and mixing characteristics are input to the kinetics code as its boundary conditions. A "nonuniform coefficient" is introduced to transform the fluid-dynamic mixing to the diffusive mixing term of the kinetics code. As a result, precise predictions of the gain distribution and laser output are given with a reasonable computational cost. The developed model is applied to the X-wing-type supersonic mixing chemical oxygen–iodine laser, which we have developed, and the calculated gain and output power are compared with the experimental results. The excellent agreements of calculated and experimental results show the validity of the developed method.

Nomenclature

C_g^2	=	rate constant of the gth second order reaction
C_h^3	=	rate constant of the hth third order reaction
D_a	=	artificial diffusion coefficient
k	=	fitting parameter of the artificial diffusion constant
M^i	=	number density of the ith species
n	=	number of primary flow layers and secondary flow layers
n_p	=	photon density
P	=	optical power
T	=	temperature of the active medium
v	=	gas velocity
x	=	coordinate lateral to the main flow (parallel to the optical axis)
y	=	vertical coordinate
z	=	coordinate to the main-flow direction
η	=	nonuniform coefficient
χ_I	=	iodine molar fraction

I. Introduction

THE chemical oxygen–iodine laser (COIL) is a high-power, efficient chemical laser operating at 1.315 μm. Because the operating wavelength is in the minimum-loss band of the silica optical fiber, high-power, long-distance fiber delivery of the laser output is possible and that makes COIL promising for applications such as mining, civil engineering, nuclear plant dismantlement, and industrial applications.

The energy source of the COIL is basic hydrogen peroxide (BHP). The gas–liquid surface reaction between BHP and chlorine gas produces electronically excited oxygen molecules, $O_2(^1\Delta)$. The $O_2(^1\Delta)$ is mixed with inert buffer gas such as nitrogen and transferred to the laser cavity under a low partial pressure (less than 2 kPa) to avoid collisional deactivation. Then the iodine molecule carried with inert gas such as nitrogen is injected into the main flow, and the mixture is supersonically expanded. The iodine is dissociated by a complex, collisional process involving $O_2(^1\Delta)$ [1]. The ratio of I_2 to O_2 is approximately 2%. Part of the energy contained in $O_2(^1\Delta)$ is used to dissociate the iodine, and the rest is used to excite iodine atoms via the near-resonant energy transfer reaction

$$O_2(^1\Delta) + I(^2P_{3/2}) \underset{kb}{\overset{kf}{\rightleftarrows}} O_2(^3\Sigma) + I(^2P_{1/2}) \tag{1}$$

where the equilibrium constant $k_f/k_b = 0.75\exp[403/T]$. Lasing occurs between excited $I(^2P_{1/2})$ and ground-state $I(^2P_{3/2})$. The overall efficiency of the COIL is measured by its "chemical efficiency," defined as the number of emitted photons divided by the number of chlorine molecules input. Supersonic expansion of the laser medium is employed mainly to achieve a high-efficiency because the gasdynamic cooling of the medium shifts the equilibrium condition of Eq. (1) to the right-hand side as indicated by

$$K_e = \frac{[O_2(^3\Sigma)][I(^2P_{1/2})]}{[O_2(^1\Delta)][I(^2P_{3/2})]} = 0.75\exp\left[\frac{403}{T}\right] \tag{2}$$

a change that results in a higher gain and more complete energy extraction from $O_2(^1\Delta)$.

In reality, the gasdynamic cooling is only one of the conditions necessary for achieving high-efficiency operation. Because of the complex chemistry occurring with a relatively slow mixing process, the efficient mixing of the primary flow (oxygen) and secondary flow (iodine) is the key to achieving high-efficiency, and several mixing schemes have been proposed to date [2–5]. Nevertheless, experimentally obtained chemical efficiency has been far less than the theoretical limit, and efforts to achieve a higher chemical efficiency are one of the main subjects of COIL research studies.

Improvements in chemical efficiency have been closely related to the modeling efforts of COIL. The model of COIL developed thus far is categorized into three types. The first type is a full kinetics model with no fluid dynamics considered [6,7]. Because the fluid-dynamic mixing of the primary flow and secondary flow plays a primary role in the building-up process of the active medium, the prediction of this type of model is quite inaccurate or qualitative. However, this type of

Received 4 October 2005; accepted for publication 22 October 2006.

*Associate Professor, Department of Physics, School of Science, 1117 Kitakaname. Member AIAA.
†Graduate Student, Department of System Design Engineering, Faculty of Science and Engineering, 3-14-1 Hiyoshi, Kohokuku.
‡Associate Professor, Department of System Design Engineering, Faculty of Science and Engineering, 3-14-1 Hiyoshi, Kohokuku.

simulation has been favored to avoid the complexity of the three-dimensional fluid dynamics involved in the COIL mixing process.

The second type of simulation is a full Navier–Stokes equation model with no or limited chemical equations [8,9]. The recent evolution of the performance of personal computers makes the use of three-dimensional full Navier–Stokes computational fluid dynamics (CFD) on them practical. Our recent successful development of what we call an "X-wing" mixing nozzle [10] greatly owes to this type of simulation. On the other hand, the calculated results of this type of simulation only indicate the degree of mixing, and no information is given for the small-signal gain or expected chemical efficiency.

The third type is a full Navier–Stokes equation CFD with a full kinetics package [11,12]. This type is much better than the previous ones, however, it has certain limitations. The combination of the full Navier–Stokes simulation with a complete set of rate equations is so computationally costly that one should employ the latest supercomputer or wait patiently for a few months to complete one case of calculation.

In this study, we aim to add the capability of laser performance prediction to the second type of simulation we have been using, without increasing computational cost considerably. To solve this problem, we have developed a hybrid simulation model that combines inert gas, full Navier–Stokes CFD code with one-dimensional, multiple-leaky-stream-tubes full kinetics code. First, the flowfield is calculated by the Navier–Stokes code. Then the resultant temperature, velocity, and mixing characteristics are fed to the kinetics model as its boundary conditions. The nonuniform coefficient is introduced to transform fluid-dynamic mixing to the diffusive mixing term of the kinetics model. This idea is justified because in a typical COIL flow, more than 70% of the flowing gas is inert buffer gas and heat release as a result of chemical reactions has a minor effect on flowfield. Therefore, the mixing characteristics, the determinative input parameter to the kinetics model, could be solved separately. On the other hand, the kinetics model could be quite well approximated with a leaky-stream-tube model once local temperature, velocity, and degree of mixing, as functions of the position in the flow are known preliminarily.

We have applied the developed simulation to the recently developed X-wing-type supersonic mixing COIL. Figure 1 shows a schematic drawing of the X-wing supersonic mixing nozzle. Thin wedges are set in an alternating fashion across the flow duct. Because those wedges resemble the letter X viewed from the side, we call this component the X-wing. The assembly of wedges primarily functions as the supersonic expansion nozzle, but also doubles as a streamwise vortex generator. The primary flow, coming from the left at a subsonic velocity, is choked at the apexes of the wedges, and the alternating configuration of the wedges generates strong streamwise vortices. The secondary flow is injected at the nozzle exit plane (NEP) perpendicularly to the main flow. The contact surface between the primary and secondary flows is immediately enlarged by the streamwise vortices, a change that should lead to rapid completion of iodine dissociation. Notably, the streamwise vortex has a much longer life than the transverse vortex in the supersonic flow, and it is the most effective factor in enhancing the mixing in the supersonic stream.

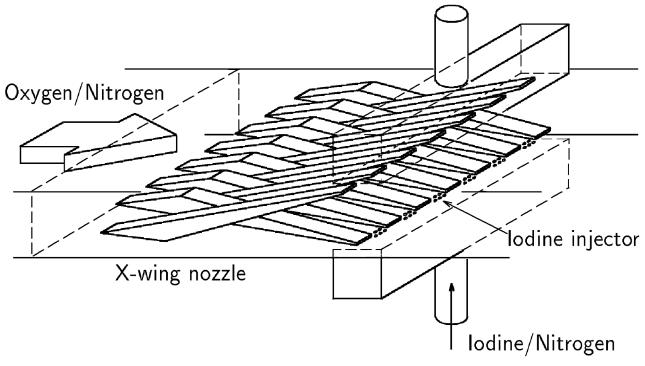

Fig. 1 Schematic drawing of X-wing supersonic mixing nozzle.

In this paper, we discuss the methodology of the proposed model and apply the model to the X-wing COIL apparatus. The calculated small-signal gain and chemical efficiency are compared with the experimental results to assess the reliability of the code.

II. Methodology of Simulation

A. Computational Fluid Dynamics Part

CFD analysis was conducted using a commercial Navier–Stokes equation solver, PHOENICS 3.5.1. Figure 2 shows the defined calculation domain of the problem. The directions of the x, y, and z coordinates are defined as in the figure. The size of the domain defined is $5 \times 25 \times 240$ mm. The upstream boundary is defined as a fixed mass flow, and the downstream boundary condition is defined as a fixed pressure. The pressure defined is set equal to that observed in the experiments. All the surfaces of the objects inside the domain are modeled as smooth, nonslipping, and adiabatic. The turbulence model is not introduced because the Reynolds number of the problem is less than 500 when the width of the wedges are defined to be the characteristic length. Different species in the flowing gas are not taken into account in the CFD part. The gas flowing in the calculation domain is assumed to be nitrogen. This is justified because more than 95% of the experimental "hot" flow comprises nitrogen and oxygen. The agreement between the calculated results and the experimentally deduced temperature and Mach number from the small-signal gain measurement was good as described in our previous paper [9].

Among the CFD results, the physical quantities used in the kinetics calculation are flow velocity, temperature, and the mixing of the primary and secondary flows as functions of position z. Because the kinetics model is one-dimensional, each quantity must be reduced to be one-dimensional. In this study, the following approach has been taken for velocity and temperature. First, the quantities are taken along the centerline depicted in Fig. 2. Next, each quantity $Q(x)$ is simply averaged over the x axis to find the average value $\bar{Q}$ as

$$\bar{Q} = \frac{\int_0^W Q(x)\,\mathrm{d}x}{W} \tag{3}$$

where W is the width of the domain.

The degree of mixing is reduced to a one-dimensional function of z by the following procedure. First, the iodine molar fraction $\chi_I(x, y)$ is averaged over the x–y plane. Next, the standard deviation of the $\chi_I(x, y)$ is calculated, and normalized by the average value as

$$\eta(z) = \frac{\sqrt{\iint[\chi_\mathrm{I}(x, y) - \bar{\chi}_\mathrm{I}]^2 \mathrm{d}x\,\mathrm{d}y}}{\bar{\chi}_\mathrm{I}} \tag{4}$$

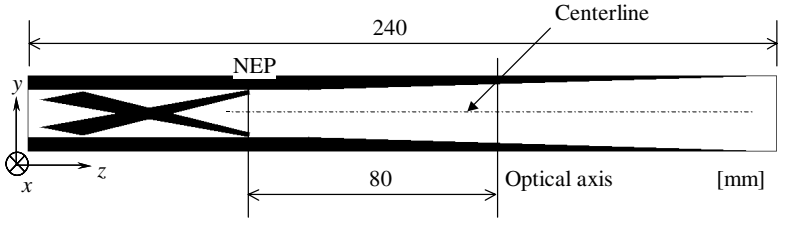

Fig. 2 Calculation domain viewed from side of flow duct.

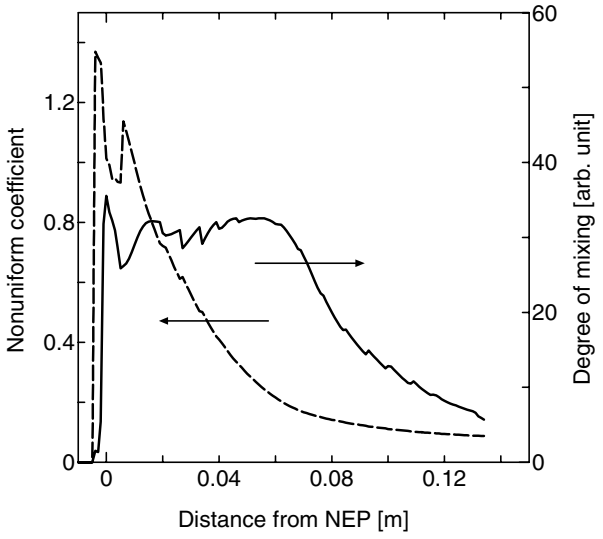

Fig. 3 Nonuniform coefficient and its derivative for typical calculation result.

where $\bar{\chi}_I$ is the average value of $\chi_I(x, y)$. The resultant quantity $\eta(z)$ is defined as the nonuniform coefficient. In our model, the artificial diffusion constant, which determines the mixing in the kinetics part, is considered proportional to the derivative of the nonuniform coefficient defined before, namely,

$$D_a \frac{\partial^2 M^i(z, y, t)}{\partial y^2} = \frac{v(z)k}{\eta(z)} \frac{d\eta(z)}{dz} \tag{5}$$

Figure 3 shows the calculated nonuniform coefficient from a typical CFD result and its derivative. A low-pass filter was applied to the derivative to eliminate the spikes and negative values. It is seen that the derivative is nearly constant from the nozzle exit plane to a position 80 mm downstream, and then it decreases rapidly. This can be explained by the fact that the mixing of the X-wing nozzle is dominated by the streamwise vortices and the CFD calculation shows that those vortices go off at approximately 80 mm downstream of the NEP.

B. Kinetics Model Part

Figure 4 shows a schematic drawing of the one-dimensional, multiple-leaky-stream-tubes kinetics model. The flowfield is divided into multiple stream tubes of oxygen layers and iodine layers. The main-flow direction and the perpendicular axis are the same as the CFD model. Downstream of the iodine injector position, diffusive mixing of adjacent layers is assumed. The artificial diffusion constant is set proportional to the derivative of the nonuniform coefficient calculated in the CFD part. The flow velocity and temperature are functions of the z coordinate, and given by the CFD results. Downstream of the iodine injector, a rooftop optical resonator is placed where the interaction of iodine atoms and photon flux is calculated. Flowfield is discretized in the z coordinate by a 1 mm grid, and in the y direction, the width of the duct is divided into primary layers and secondary layers whose widths are determined with respect to the molar flow rates. The minimum number of layers is sought in which the result of calculation is not considerably affected by the discretization. Both top and bottom boundaries in Fig. 4 are assumed to be symmetric boundaries. Therefore, layer zero represents the center of the duct, while the $(2n-1)$th layer represents the top and bottom walls of the flow duct.

The partial differential equation governing the flowfield is as follows.

$$\begin{aligned}\frac{\partial M^i(z, y, t)}{\partial t} &= \sum_g C_g^2[T(z, y, t)]M^j(z, y, t)M^k(z, y, t) \\ &+ \sum_h C_h^3[T(z, y, t)]M^o(z, y, t)M^p(z, y, t)M^q(z, y, t) \\ &- \frac{\partial}{\partial z}[M^i(z, y, t)H(z)v(z)]\frac{1}{H(z)} - D_a \frac{\partial^2 M^i(z, y, t)}{\partial y^2} - \delta \frac{\partial n_p(z, t)}{\partial t}\end{aligned} \tag{6}$$

Here, $H(z)$ is the height of the duct in centimeters, and $v(z)$ is the gas velocity at the position z (cm/s). If i represents the upper state of the iodine atom, then $\delta = 1$; if i represents the ground state of the iodine atom, then $\delta = -1$; $\delta = 0$ for the other cases. The first two terms of the right-hand side represent chemical reactions of the second and third orders, the next two terms represent the gas flow and mixing, respectively, and the last term represents the change of the iodine upper and lower states by the stimulated emission.

The fitting of the artificial diffusion constant to the nonuniform coefficient is conducted as follows. First, $\eta(z)$ is differentiated,

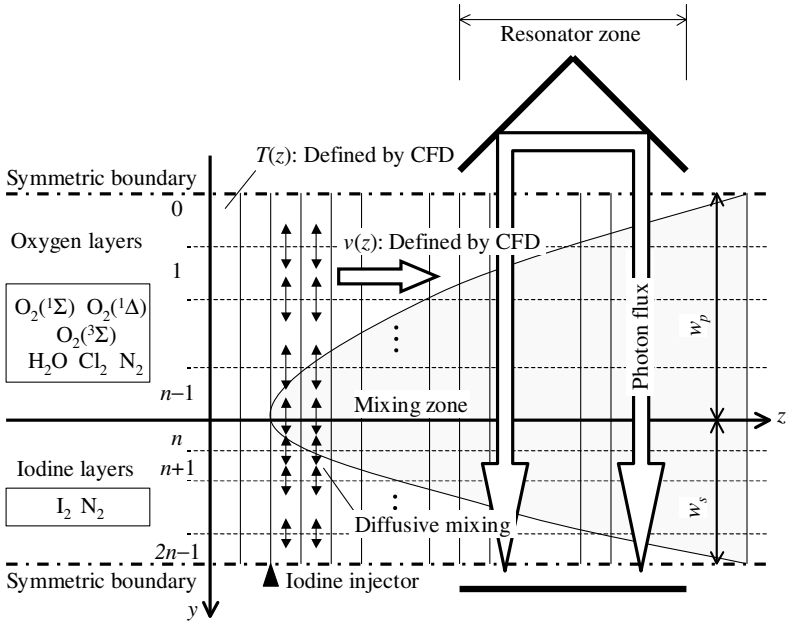

Fig. 4 Schematic drawing of one-dimensional multiple-leaky-stream-tubes kinetics model.

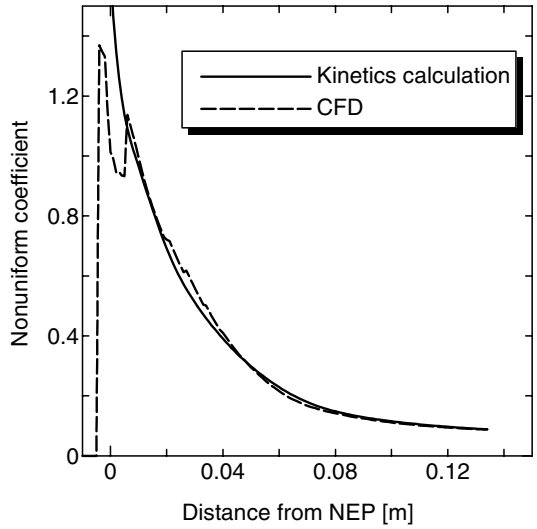

Fig. 5 Comparison of nonuniform coefficient after fitting of constant k has been completed.

$d\eta/dz$ is multiplied by an arbitrary constant k, and substituted to $D_a[\partial^2 M^i(z, y, t)/\partial y^2]$ in accordance with Eq. (5) to give the diffusion term. Then, $\eta(z)$ is calculated again in the kinetics simulation based on the diffusive mixing, and the result is compared with the CFD result. The kinetics simulation is repeated by changing the constant k, until reasonable agreement of $\eta(z)$ between CFD and kinetics simulation is met. Figure 5 shows the $\eta(z)$ calculated by CFD and by kinetics code as a result of the fitting operation. The method presented is justified from the comparison of two traces because a quite good matching is obtained by only changing the constant k in Eq. (5).

The resonator intensity is determined by the following procedure. First, the temporary photon density increase rate is calculated by the photon rate equation as follows.

$$\frac{\partial n'_p(z,t)}{\partial t} = \frac{P(z,t)}{h\nu}\left[\sum_y \sigma(T)\frac{7}{12}\left([\mathrm{I}^*](z,y,t) - \frac{1}{2}[\mathrm{I}](z,y,t)\right) - L_g\right] + \varepsilon_r[\mathrm{I}^*](z,y,t) \tag{7}$$

Here, $\partial n'_p(z,t)/\partial t$ is the change rate of the local photon density ($1/\mathrm{cm}^3 \cdot \mathrm{s}$), $P(z,t)$ is the intensity of the resonant mode ($\mathrm{W/cm}^2$), $\sigma(T)$ (cm^2) is the stimulated emission cross section of the $\mathrm{I}^* \rightarrow \mathrm{I}$ transition, L_g is the resonator loss ($1/\mathrm{cm}$), and ε_r represents the fraction of the spontaneous emission that adds effectively to the oscillating mode. Here, ε_r is defined as

$$\varepsilon_r = \frac{D_m D_h}{4\pi L^2} \cdot \frac{7}{12} \cdot A_{21(3\text{–}4)} \tag{8}$$

where D_m and D_h, respectively, represent the mirror dimensions of the flow direction and duct height, L is the resonator length, and $A_{21(3\text{–}4)}$ is the Einstein's A-coefficient of the (3–4) hyperfine sublevels transition. In the second step, the photon increase rate is averaged as the rule of the rooftop resonator.

$$\frac{\partial n_p[(z_0 - z), t]}{\partial t} = \frac{\partial n_p[(z_0 + z), t]}{\partial t} = \frac{1}{2}\left(\frac{\partial n'_p[(z_0 - z), t]}{\partial t} + \frac{\partial n'_p[(z_0 + z), t]}{\partial t}\right) \tag{9}$$

Here, z_0 represents the center position of the resonator mirror. The sum of the circulating power in both directions is readily calculated as $P = n_p chv$.

The differential equation is discretized by the upwind finite difference method. The upstream boundary condition is given by the equations

$$M^i(0,t) = M_0^i \tag{10}$$

The difference equation is explicitly integrated in the time domain with first-order accuracy.

The rate equation set used in this work is shown in Table 1. It is based on the U.S. Air Force standard rate equation package [13], and rates relevant to nitrogen and three-body recombination of iodine are included.

As a preliminary calculation, the number of layers for both oxygen and iodine is determined by conducting calculations with different numbers of layers. Figure 6 shows the small-signal gain of the layer zero as a function of the position along the flow. As seen in the figure, the calculated gain distribution is almost unchanged when the number of layers is five or larger. Therefore, we determined the number of layers as five.

III. Experimental Setup

Figure 7 shows the experimental setup. The apparatus consists of a fuel handling system, a liquid-jet singlet oxygen generator (SOG), an X-wing nozzle, iodine injectors, a laser cavity, a vacuum pump system, and measurement devices. The BHP, delivered to the SOG using atmospheric air pressure, contains 6.5 mol/l of HO_2^- ion; its temperature is maintained at 255 K. The SOG used in this work is the same one as discussed in earlier reports on the high-efficiency supersonic COIL with nitrogen as a buffer gas [14] and high-pressure subsonic operation [15]. A gas transport duct connects the SOG and the nozzle section. A buffer gas injector is inserted across the duct to inject nitrogen gas. As in previous studies [14,15], buffer gas precooling is employed to enhance output power by assisting the gasdynamic cooling of the laser medium. An X-wing nozzle is placed at the end of the transport duct, as shown in Fig. 1. It consists of 15 wedges, each 5 mm wide, 5 mm high, and 68 mm long. The alternating wedges are tilted by ± 12 deg from the horizontal. Iodine injector holes, 0.6 mm in diameter, are drilled into the top and bottom walls, at the NEP of the X-wing nozzle. As seen in Fig. 1, holes are placed between two adjacent wedges.

The optical resonator is 50 cm long and consists of two mirrors with 5 m curvatures. The sum of the transmission by the two mirrors is varied from 0.4 to 4%. The gain length is 75 mm and the distance between the NEP and the optical axis is 80 mm. The height of the laser duct is 15 mm at the NEP and gradually expands at an angle of ± 2 deg to compensate for the boundary layer.

The vacuum system consists of a two-stage Roots blower, a steam ejector, and a water-ring pump. The effective volume flow rate under the operating conditions is approximately 1000 l/s.

The Cl_2 and nitrogen gas flows are controlled by digital mass flow controllers (STEC SEC-4600). The I_2 flow rate is measured by absorption spectroscopy ($\lambda = 633$ nm). The laser output power from the two mirrors is monitored by two power meters (Coherent: Model 5000 and Ophir: FL250-A).

In all the experiments, the Cl_2 flow rate was fixed at 20.0 mmol/s. The chlorine utilization was measured to be 90%, and the yield was measured to be 70% in our previous study [16]. The primary buffer flow rate was 50.0 mmol/s, and that of the iodine carrier was 13.8 mmol/s. The I_2/O_2 titration was controlled to be $1.4 \pm 0.1\%$. When the primary buffer was not cooled, the stagnation temperature was 300 K, however, it went down to 268 K when precooling was applied.

The small-signal gain of the active medium was measured using a distributed feedback laser diode (DFB-LD) as a probe beam. Figure 8 shows the block diagram of the measurement setup. A frequency-modulated DFB-LD beam is split into two parts by a half-mirror and one half of the beam makes a round trip of the active medium. The other half of the beam is used to monitor the wavelength. The wavelength of the probe is tuned to the (3–4) hyperfine transition of the iodine $^2P_{1/2} - {}^2P_{3/2}$ system, and the wavelength modulation

Table 1 Rate equation package used in kinetics simulation

Reaction		Rate constant, cm^3/s	No.
$O_2(^1\Delta) + O_2(^1\Delta)$	$\rightarrow O_2(^1\Sigma) + O_2(^3\Sigma)$	$9.5 \times 10^{-28} T^{3.8} \exp(700/T)$	1
$O_2(^1\Delta) + I$	$\rightarrow O_2(^3\Sigma) + I^*$	$2.3 \times 10^{-8} T^{-1}$	2
$O_2(^3\Sigma) + I^*$	$\rightarrow O_2(^1\Delta) + I$	$3.07 \times 10^{-8} T^{-1} \exp(402/T)$	3
$O_2(^1\Delta) + I^*$	$\rightarrow O_2(^1\Sigma) + I^*$	$4.0 \times 10^{-24} T^{3.8} \exp(700/T)$	4
$O_2(^1\Sigma) + N_2$	$\rightarrow O_2(^1\Delta) + N_2$	2.2×10^{-15}	5
$O_2(^1\Delta) + N_2$	$\rightarrow O_2(^3\Sigma) + N_2$	1.4×10^{-19}	6
$I^* + N_2$	$\rightarrow I + N_2$	6.5×10^{-17}	7
$I_2^* + N_2$	$\rightarrow I_2 + N_2$	8.8×10^{-12}	8
$I^* + O_2(^1\Delta)$	$\rightarrow I + O_2(^1\Delta)$	1.1×10^{-13}	9
$O_2(^1\Sigma) + O_2(^3\Sigma)$	$\rightarrow O_2(^1\Delta) + O_2(^3\Sigma)$	4.6×10^{-17}	10
$O_2(^1\Delta) + O_2(^3\Sigma)$	$\rightarrow O_2(^3\Sigma) + O_2(^3\Sigma)$	1.6×10^{-18}	11
$I^* + O_2(^3\Sigma)$	$\rightarrow I + O_2(^3\Sigma)$	4.6×10^{-14}	12
$I_2^* + O_2(^3\Sigma)$	$\rightarrow I_2 + O_2(^3\Sigma)$	5.0×10^{-11}	13
$O_2(^1\Delta) + I$	$\rightarrow O_2(^3\Sigma) + I$	1.0×10^{-15}	14
$I^* + I$	$\rightarrow I + I$	1.6×10^{-14}	15
$O_2(^1\Sigma) + H_2O$	$\rightarrow O_2(^1\Delta) + H_2O$	6.7×10^{-12}	16
$O_2(^1\Delta) + H_2O$	$\rightarrow O_2(^3\Sigma) + H_2O$	4.0×10^{-18}	17
$I^* + H_2O$	$\rightarrow I + H_2O$	2.0×10^{-12}	18
$I_2^* + H_2O$	$\rightarrow I_2 + H_2O$	3.0×10^{-10}	19
$O_2(^1\Sigma) + Cl_2$	$\rightarrow O_2(^1\Delta) + Cl_2$	4.5×10^{-16}	20
$O_2(^1\Delta) + Cl_2$	$\rightarrow O_2(^3\Sigma) + Cl_2$	6.0×10^{-18}	21
$I^* + Cl_2$	$\rightarrow I + Cl_2$	2.0×10^{-14}	22
$O_2(^1\Sigma) + I_2$	$\rightarrow O_2(^3\Sigma) + I_2$	1.6×10^{-11}	23
$O_2(^1\Delta) + I_2$	$\rightarrow O_2(^3\Sigma) + I_2^*$	7.0×10^{-15}	24
$I^* + I_2$	$\rightarrow I + I_2^*$	$1.4 \times 10^{-13} \exp(1660/T)$	25
$I^* + Cl_2$	$\rightarrow Cl + ICl$	5.5×10^{-15}	26
$I^* + ICl$	$\rightarrow I_2 + Cl$	1.5×10^{-11}	27
$I_2 + Cl$	$\rightarrow I + ICl$	2.0×10^{-10}	28
$Cl + ICl$	$\rightarrow I + Cl_2$	8.0×10^{-12}	29
$I_2 + O_2(^1\Sigma)$	$\rightarrow I + I + O_2(^1\Delta)$	4.0×10^{-12}	30
$I_2^* + O_2(^1\Delta)$	$\rightarrow I + I + O_2(^3\Sigma)$	3.0×10^{-10}	31
$I_2^* + I + I$	$\rightarrow I_2 + I_2$	3.6×10^{-30}	32
$I_2 + I^* + I$	$\rightarrow I_2 + I_2$	3.6×10^{-30}	33
$O_2(^3\Sigma) + I^* + I$	$\rightarrow O_2(^3\Sigma) + I_2$	3.7×10^{-32}	34
$N_2 + I^* + I$	$\rightarrow N_2 + I_2$	4.2×10^{-32}	35

width is set sufficiently to measure the full linewidth of the transition. The position of the probe beam can be varied horizontally over the width of the optical aperture, ±50 mm centered at 80 mm from the NEP.

IV. Results and Discussion

A. Determination of Iodine/Oxygen Titration

In our experimental setup, measurement of absolute iodine flow rate maybe inaccurate because of the lack of precise calibration. We conducted small-signal gain measurements and compared the results with calculations where the same conditions, varying I_2/O_2 titration as a parameter to find the appropriate I_2/O_2 titration that matches the simulation results to the measurement results. Figure 9 shows the result. The lines show the small-signal gain of layer zero as a function of z. It is reasonable to compare the measured gain with the calculated gain of layer zero because gain measurements were conducted along the centerline of the flow duct. In the calculations, I_2/O_2 ratio was varied from 0.8 to 1.2%. Approximate linear dependencies of the absolute gain as functions of iodine flow rate are observed. The experimental results are in very good agreement with the calculation of $I_2/O_2 = 1.0\%$ case. From this result, we concluded that our measurement of iodine flow rate was overestimated. In part, the discrepancy may come from the fact that the kinetics model did not incorporate the fluid-dynamic mixing effect. In reality, fluid-dynamic mixing results in locally higher iodine concentration along the centerline, and higher gain than the assumption of one-dimensional diffusive mixing.

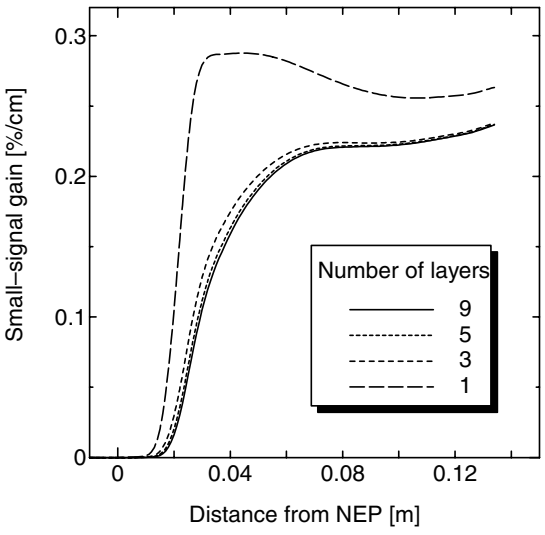

Fig. 6 Small-signal gain of layer zero as function of position along flow.

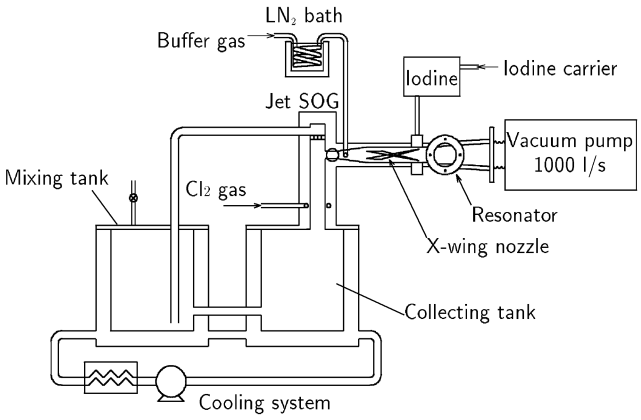

Fig. 7 Schematic drawing of experimental setup.

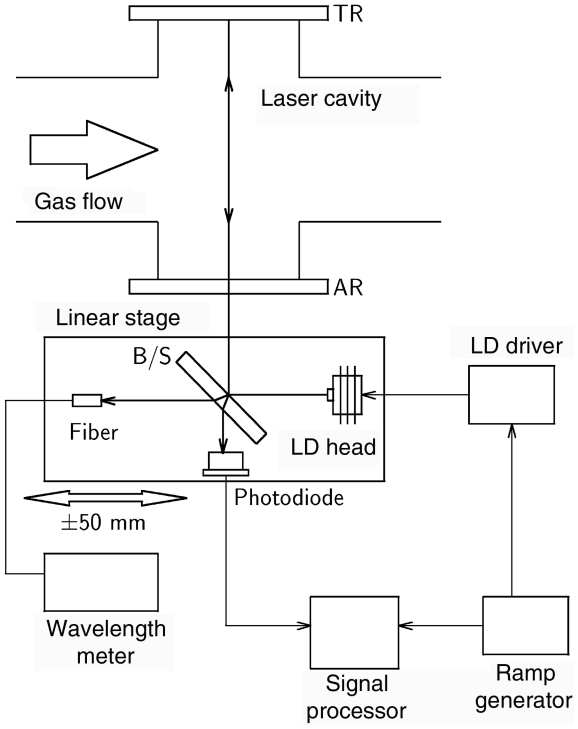

Fig. 8 Block diagram of small-signal gain measurement setup.

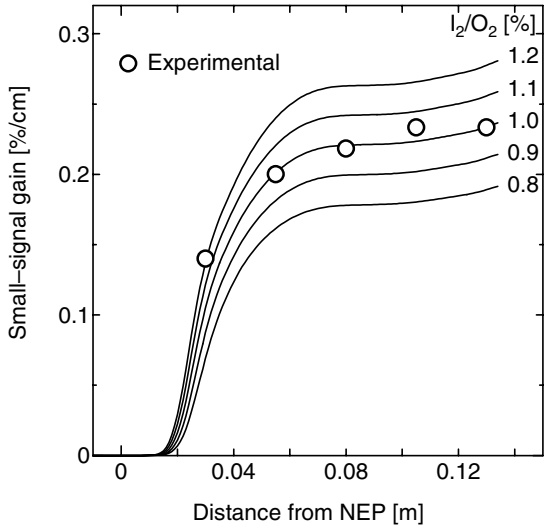

Fig. 9 Measured and calculated gain profiles along centerline and layer zero, respectively.

Nevertheless, the calculated buildup position and the trend of the gain along the centerline are in very good agreement with the measured results. This fact indicates that the mixing process was precisely reproduced using the proposed simulation.

B. Effect of Buffer Gas Precooling

Calculated gain and laser output power were compared with the experimental results for both room temperature and precooled buffer gases to see if the simulation could reproduce the effect of buffer gas precooling. First, the small-signal gains were compared. Figure 10 shows the results. The calculation conditions were set at the same values as the experimental conditions, except that the I_2/O_2 ratio was set at 1.0%. By the buffer gas precooling, it was experimentally observed that the buildup of the gain shifts upstream and the absolute value of the small-signal gain was enhanced by approximately 20% at the optical axis position. The calculated profile of the small-signal

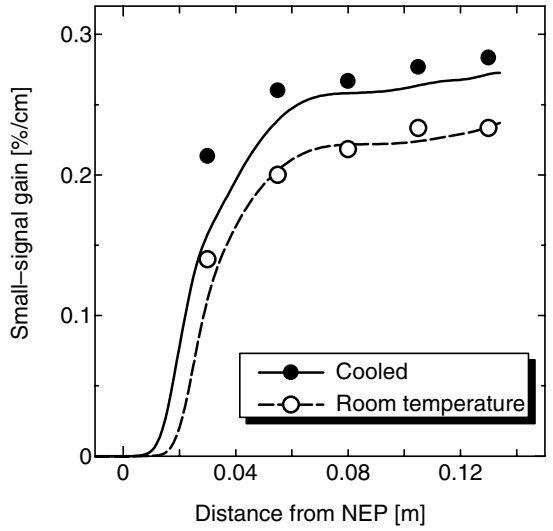

Fig. 10 Comparison of gain buildup for measured and calculated results.

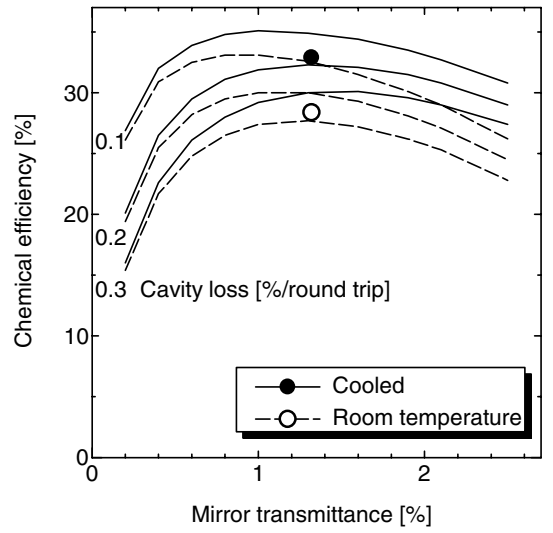

Fig. 11 Comparison of experimentally obtained laser output and model calculation.

gain at the layer zero is in very good agreement with the observations along the centerline as observed.

Next, laser output was calculated and compared with the experimental results. The experimentally obtained maximum chemical efficiency for precooled and room temperature cases were 32.9 and 28.4%, respectively, when total mirror transmittance was 1.32%. We have tried to make a Rigrod curve by varying mirror transmittance and estimating the loss of the resonator, however, it was unsuccessful because the loss of the mirrors was not constant due to the damages of the mirror surfaces caused by the lasing operations. Nevertheless, it was deduced in the range of 0.1–0.4% per round trip from the measured data. We could only compare the experimentally obtained maximum chemical efficiency with calculations in which the loss of the optical resonator was varied as a parameter. Figure 11 shows the results. The solid lines represent the results for precooled buffer gas, and dashed lines represent the results for room temperature buffer gas. The loss of the resonator was varied as 0.1, 0.2, and 0.3% per round trip. For the precooled case, the experimental result coincides with the calculated result of 0.18% loss. For the room temperature case, experimentally obtained output power coincides with the calculated results of 0.26% loss. Both cases are in reasonable agreement with the experimentally deduced loss with mirror transmittance variation. Because the chemical efficiency was reproduced for both precooled and room temperature buffer gases

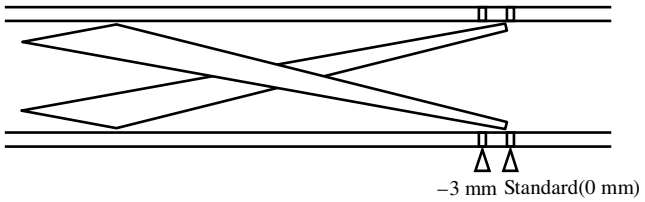

Fig. 12 Position shift of iodine injectors.

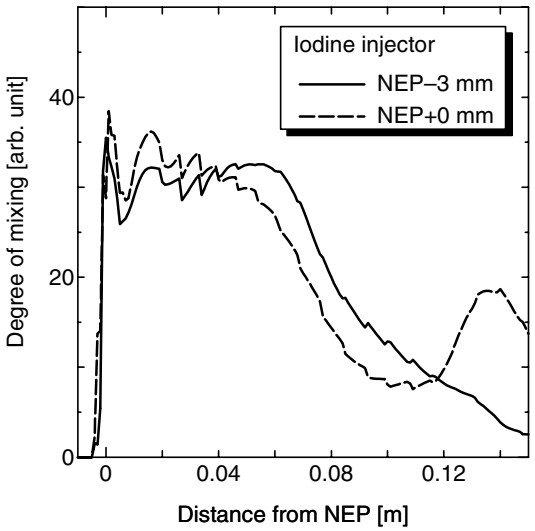

Fig. 13 Comparison of calculated degree of mixing for standard and upstream iodine injectors.

with a reasonable assumption of optical resonator loss, the accuracy of the proposed model is verified again with those comparisons.

C. Varying Mixing Efficiency

It was observed that changing the position of the iodine injectors with respect to the X-wing nozzle results in a significant change in mixing characteristics. To check if the model reproduces the phenomenon that would occur, we conducted both experiments and calculations with shifted iodine injector positions. In the standard setup, the iodine injectors were placed just beneath the X-wing nozzle tips. We have set back the iodine injectors by 3 mm as shown in Fig. 12, and conducted experiments and calculations. Visually, the disappearance of the yellow fluorescence caused by the $I_2(B-X)$ transition shifts upstream by the shift of the iodine injectors. The fast disappearance of the $I_2(B-X)$ fluorescence is a sign of the fast completion of mixing. In the CFD calculations, the fast completion of mixing was observed as expected. This change was mainly due to the deeper penetration of the iodine jet to the center of the duct by changing the position of the injectors to the place where the z-direction momentum of the main flow is smaller. As a result, the calculated nonuniform coefficient was changed. Figure 13 shows the comparison of the derivative of the nonuniform coefficient, namely, the degree of mixing for the standard case and shifted case. In the shifted configuration, the degree of mixing at the most critical section of gain buildup is higher than that in the standard case. That should result in a positive effect on laser performance.

Figure 14 shows a comparison of the experimentally measured and calculated small-signal gains. For calculations, I_2/O_2 was set at 1.0%. In the experimental result, the small-signal gain at 55 mm from NEP was approximately 30% higher than in the standard case, and the peak position of the gain shifted upstream. As discussed earlier, the shift of the gain peak can be explained by the fast completion of the mixing. On the other hand, the higher peak value is not solely explained by the fast completion of the mixing. The simulation results indicated "layer zero" in the figure and also showed the shift

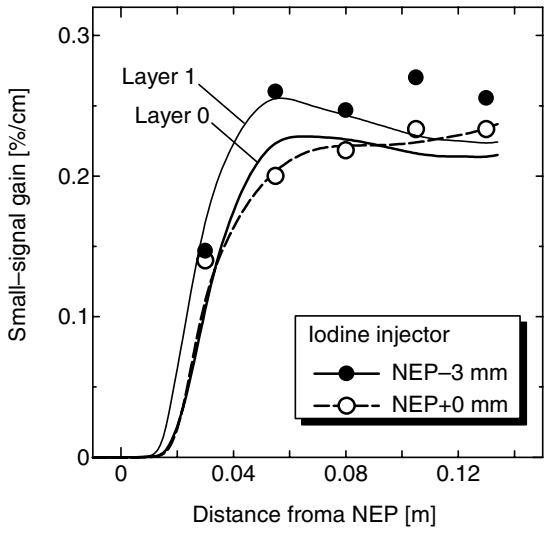

Fig. 14 Comparison of gain buildup for measured and calculated results.

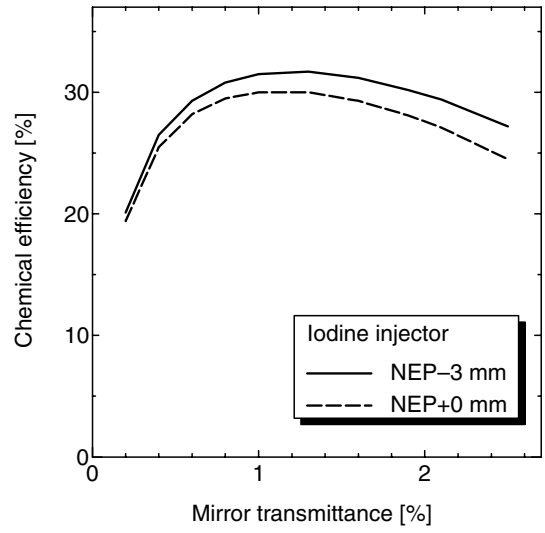

Fig. 15 Predicted laser output for both iodine injector positions.

of the peak position, however, the peak value was not different to that in the standard case. It is interesting to examine the gain buildup of layer one as seen in the figure. It is higher than layer zero, and the profile is in very good agreement with the measured gain. The explanation of this fact is as follows: because the hydrodynamic mixing is stronger in the shifted case, the uniformity of the local iodine concentration along the centerline was less than in the standard case. Hence, the measured gain on the centerline is more affected by the nonuniformity of the iodine concentration than in the standard case, which results in a 30% higher peak gain at the front edge of the optical aperture. As the flow becomes uniform downstream, the discrepancy decreases as seen in the figure.

The laser oscillation experiments for the shifted iodine injectors have not been conducted yet with the best mirrors, because they were damaged. Nevertheless, an output power approximately 5% higher than that in the standard case was obtained, under the same optical resonator conditions. The result of laser oscillation simulation is shown in Fig. 15. The solid line represents the result for the shifted iodine injector, whereas the dashed line represents the result for the standard case. The cavity loss was assumed to be 0.2%. The model predicts that the chemical efficiency with the nozzle shift by 3 mm should obtain an output 5% higher than that in the standard case. That is again in very good agreement with the experimental observation.

V. Conclusions

A hybrid simulation for supersonic chemical oxygen–iodine lasers has been proposed and the validity of the proposed method was checked by comparing the calculated results with the experimental results. The model comprises a three-dimensional Navier–Stokes equation solver without implementing a kinetics model and a detailed kinetics simulation with a multiple-leaky-stream-tubes model. In the past, most COIL simulations were detailed rate-equation models with no fluid dynamics treatment or detailed fluid dynamics models with limited or no kinetics involved, due to the limitation of computational resources. In the proposed method, the flowfield of the supersonic COIL was precisely modeled using a full Navier–Stokes equation, and the resultant temperature, velocity, and mixing characteristics information was fed as boundary conditions of the kinetics model. As a result, accurate predictions of the gain and laser output were possible with a reasonable computational cost. The developed model was applied to the X-wing-type supersonic mixing COIL we have developed. To reduce the fluid-dynamic mixing to the one-dimensional diffusive mixing term used in the kinetics part, a nonuniform coefficient was defined and its derivative was used to define the artificial diffusion constant in the kinetics model. The predicted small-signal gain along the flow well reproduced the experimentally measured values. The prediction of the gain enhancement by the buffer gas precooling quantitatively agreed with the observed results for both the magnitude and change in the functional shape of gain along the flow. The predicted laser output by the proposed simulation under the assumption of the 0.2% cavity loss matched the experimental result. When the iodine injector was shifted 3 mm upstream, the rapid completion of the mixing was evident by the observation of the iodine $(B - X)$ fluorescence. The phenomenon was verified by CFD and the reason for this mixing enhancement was understood as the deeper penetration of the iodine jet in the main flow. The proposed model successfully reproduced the observed change in magnitude and the profile of the gain along the flow. In conclusion, the excellent agreements of experimental and calculated results showed the reliability of the developed simulation method.

Acknowledgments

The authors are grateful to Kawasaki Heavy Industries, Ltd., for assistance in conducting the experiments, and for allowing us to use their vacuum system and measurement equipment. The authors are also grateful to CHAM-Japan for supporting the computational fluid dynamics calculations.

References

[1] Heidner, R. F., III, Gardner, C. E., Segal, G. I., and El-Sayed, T. M., "Chain-Reaction Mechanism for I_2 Dissociation in the $O_2(^1\Delta)$-I Atom Laser," *Journal of Physical Chemistry*, Vol. 87, No. 13, 1983, pp. 2348–2360.

[2] Nikolaev, V. D., "Comparative Analysis of the Different Methods of Preparing Active Media in a Supersonic COIL," *Gas and Chemical Lasers and Intense Beam Applications*, SPIE: International Society for Optical Engineering, Vol. 3268, May 1998, pp. 157–162.

[3] Endo, M., Sugimoto, D., Okamoto, H., Nanri, K., Uchiyama, T., Takeda, S., and Fujioka, T., "Output Power Enhancement of a Chemical Oxygen–Iodine Laser by Predissociated Iodine Injection," *Japanese Journal of Applied Physics*, Vol. 39, No. 2A, 2000, pp. 468–474.

[4] Vyskubenko, B. A., Adamenkov, A. A., Bakshin, V. V., Buzoverya, V. V., Vdovkin, L. A., Deryugin, Y. N., Efremov, V. I., Ilyin, S. P., Kalinovskiy, V. V., Kolobyanin, Y. V., Konovalov, V. V., Kudryashov, E. A., Moiseev, V. B., and Nickolaev, V. D., "Oxygen–Iodine Laser in Russian Federal Nuclear Center VNIIEF," *XV International Symposium on Gas Flow, Chemical Lasers, and High-Power Lasers*, SPIE: International Society for Optical Engineering, Vol. 5777, March 2005, pp. 96–99.

[5] Rybalkin, V., Katz, A., Barmashenko, D., and Rosenwaks, S., "33% Efficient Chemical Oxygen–Iodine Laser with Supersonic Mixing of Iodine and Oxygen," *Applied Physics Letters*, Vol. 82, No. 22, 2003, pp. 3838–3840.

[6] Copeland, D. A., and Bauer, A. H., "Optical Saturation and Extraction from the Chemical Oxygen–Iodine Laser Medium," *IEEE Journal of Quantum Electronics*, Vol. 29, No. 9, 1993, pp. 2525–2539.

[7] Bruins, E., Furman, D., Rybalkin, V., Barmashenko, B. D., and Rosenwaks, S., "One-Dimensional Modeling of the Gain and Temperature in a Supersonic Chemical Oxygen Iodine Laser with Transonic Injection of Iodine," *IEEE Journal of Quantum Electronics*, Vol. 38, No. 4, 2002, pp. 345–352.

[8] Yang, T. T., Dickerson, R. A., Moon, L. F., and Hsia, Y. S., "High Mach Number, High Pressure Recovery COIL Nozzle Aerodynamic Experiments," *AIAA 31st Plasmadynamics and Lasers Conference*, AIAA Paper 2000-2425, 2000.

[9] Endo, M., Masuda, T., and Uchiyama, T., "Supersonic Chemical Oxygen–Iodine Laser with X-Shaped Streamwise Vortex Generator," *IEEE Journal of Quantum Electronics*, Vol.42, No. 1, 2006, pp. 71–77.

[10] Endo, M., Osaka, T., and Takeda, S., "High-Efficiency Chemical Oxygen Iodine Laser Using a Streamwise Vortex Generator," *Applied Physics Letters*, Vol. 84, No. 16, 2004, pp. 2983–2985.

[11] Masuda, W., Hishida, M., and Abe, Y., "Numerical Simulation of a Supersonic Mixing Chemical Oxygen–Iodine Laser with Ramp Nozzle Arrays," *XII International Symposium on Gas Flow and Chemical Lasers and High-Power Laser Conference*, SPIE: International Society for Optical Engineering, Vol. 3574, Dec. 1998, pp. 584–591.

[12] Madden, T. J., and Hager, G. D., "Investigation of Supersonic Mixing for the Chemical Oxygen–Iodine Laser (COIL)," *AIAA 30th Plasmadynamics and Lasers Conference*, AIAA Paper 99-3429, 1999.

[13] Perram, G. P., and Hager, G. D., "Standard Chemical Oxygen–Iodine Laser Kinetics Package," Air Force Weapons Lab. TR-88-50, 1988.

[14] Endo, M., Nagatomo, S., Takeda, S., Zagidullin, M. V., Nikolaev, V. D., Fujii, H., Wani, F., Sugimoto, D., Sunako, K., Nanri, K., and Fujioka, T., "High-Efficiency Operation of Chemical Oxygen–Iodine Laser Using Nitrogen as Buffer Gas," *IEEE Journal of Quantum Electronics*, Vol. 34, 1998, pp. 393–398.

[15] Wani, F., Endo, M., and Fujioka, T., "High-Pressure, High-Efficiency Operation of a Chemical Oxygen–Iodine Laser," *Applied Physics Letters*, Vol. 75, No. 20, 2000, pp. 3081–3085.

[16] Wani, F., Endo, M., Vyskubenko, B., Ilyn, S., Krukovsky, I., Takeda, S., and Fujioka, T., "Parametric Study of a Twisted Aerosol-Type Singlet Oxygen Generator," *IEEE Journal of Quantum Electronics*, Vol. 34, No. 11, 1998, pp. 2130–2137.

G. Candler
Associate Editor